C. R. Geoscience 343 (2011) 558–570

Contents lists available at ScienceDirect

Comptes Rendus Geoscience

www.sciencedirect.com

Internal geophysics (Physics of Earth's interior)

Ambient noise tomography with a large seismic array

Tomographie à partir de bruit ambiant à l'aide d'un vaste réseau sismique

Michael H. Ritzwoller *, Fan-Chi Lin, Weisen Shen

Center for Imaging the Earth's Interior, Department of Physics, University of Colorado, CO 80309-0390, Boulder, USA

ARTICLE INFO

Article history:
Received 31 August 2010
Accepted after revision 10 April 2011
Available online 21 June 2011

Written on invitation of the Editorial Board.

Keywords:
Seismology
Ambient noise
Tomography
Surface waves

ABSTRACT

The emergence of large-scale arrays of seismometers across several continents presents the opportunity to image the Earth's structure at unprecedented resolution, but methods must be developed to exploit the capabilities of these deployments. The capabilities and limitations of a method called "eikonal tomography" applied to ambient noise data are discussed here. In this method, surface wave wavefronts are tracked across an array and the gradient of the travel time field produces estimates of phase slowness and propagation direction. Application data from more than 1000 stations from EarthScope USArray in the central and western US and new Rayleigh wave isotropic and anisotropic phase velocity maps are presented together with an isotropic and azimuthally anisotropic 3D Vs model of the crust and uppermost mantle. As a ray theoretic method, eikonal tomography models bent rays but not other wavefield complexities. We present evidence, based on the systematics of an observed 1ψ component of anisotropy that we interpret as anisotropic bias caused by backscattering near an observing station, that finite frequency phenomena can be ignored in ambient noise tomography at periods shorter than $\sim$ 40 to 50 s. At longer periods a higher order term based on wavefront amplitudes or finite frequency sensitivity kernels must be introduced if the amplitude of isotropic anomalies and the amplitude and fast-axis direction of azimuthal anisotropy are to be determined accurately.

Mots clés :
Sismologie
Bruit ambiant
Tomographie
Ondes de surface

RÉSUMÉ

L'émergence de réseaux de sismomètres sur une grande échelle au travers de plusieurs continents donne l'opportunité de représenter la structure de la Terre avec une résolution jamais atteinte, mais des méthodes doivent être créées pour exploiter les possibilités de ces déploiements. Les possibilités et les limites d'une méthode appelée « tomographie de l'eikonal » appliquée aux données de bruit ambiant sont discutées ici. Dans cette méthode, les fronts d'onde des ondes de surface sont suivis au travers d'un réseau et le gradient du temps de trajet fournit des estimations de lenteur de phase et de direction de propagation. L'application a été réalisée avec des données de plus de 1000 stations de *l'EarthScope USArray* dans le Centre et l'Ouest des États-Unis et de nouvelles cartes de vitesse de phase d'ondes de Rayleigh isotrope et anisotrope, ainsi qu'un modèle Vs 3D isotrope et azimuthalement anisotrope sont présentés pour la croûte et le manteau supérieur. En tant que basée sur la théorie des rais, la tomographie de l'eikonal modélise les rais courbes, mais aucune autre des complexités du champ d'ondes. Nous présentons l'évidence, fondée sur la systématique d'une composante 1ψ observée d'anisotropie – que nous interprétons comme une anisotropie biaisée, due à une rétrodiffusion près de la station d'observation – que les phénomènes de fréquence finie peuvent être ignorés dans la tomographie à partir

* Corresponding author.
E-mail address: michael.ritzwoller@colorado.edu (M.H. Ritzwoller).

1631-0713/$ – see front matter
doi:10.1016/j.crte.2011.03.007

du bruit ambiant, pour des périodes plus courtes que ~40 à 50 s. Pour des périodes plus longues, un terme d'ordre supérieur, basé sur les amplitudes des fronts d'onde ou sur les noyaux de sensibilité à fréquence finie doit être introduit, si l'amplitude des anomalies isotropes, ainsi que l'amplitude et la direction d'axe rapide de l'anisotrope azimuthale doivent être déterminées de manière précise.

1. Introduction

The use of ambient noise to extract surface wave empirical Green's functions (EGFs) and to infer Rayleigh (Sabra et al., 2005; Shapiro and Campillo, 2004; Shapiro et al., 2005) and Love wave (Lin et al., 2008) group and phase speeds in continental areas is now well established. Phase and group velocity tomography to produce dispersion maps have been performed around the world (e.g. US: Bensen et al., 2008; Ekström et al., 2009; Moschetti et al., 2007; Asia: Cho et al., 2007; Fang et al., 2010; Kang and Shin, 2006; Li et al., 2009; Yang et al., 2010; Yao et al., 2006, 2009; Zheng et al., 2008, 2010a; Europe: Villaseñor et al., 2007; Yang et al., 2007; New Zealand and Australia: Arroucau et al., 2010; Lin et al., 2007; Saygin and Kennett, 2010; Ocean bottom and islands: Gudmundsson et al., 2007). Ambient noise tomography is typically performed at periods from about 8 s to 40 s, but the method has been applied successfully at global scales above 100 s period (Nishida et al., 2009). It has also been used to obtain information about attenuation (Lin et al., in press; Prieto et al., 2009) and body wave (Gerstoft et al., 2008; Landes et al., 2010; Roux et al., 2005; Zhan et al., 2010) and overtone signals have also been recovered (Nishida et al., 2008). Numerous three-dimensional models of the crust and uppermost mantle have emerged from surface wave analyses for isotropic shear velocity structure (e.g. US: Bensen et al., 2009; Liang and Langston, 2008; Moschetti et al., 2010b; Stachnik et al., 2008; Yang et al., 2008b; Yang et al., 2011; Asia: Guo et al., 2009; Nishida et al., 2008; Sun et al., 2010; Yao et al., 2008; Zheng et al., 2010b; Europe: Li et al., 2010; Stehly et al., 2009; New Zealand and Australia: Behr et al., 2010; Ocean bottom and islands: Brenguier et al., 2007; Harmon et al., 2007; Africa: Yang et al., 2008a), radial anisotropy (Moschetti et al., 2010a), and azimuthal anisotropy (Lin et al., 2011a; Yao et al., 2010). EGFs have also been applied to improve epicentral locations (Barmin et al., 2011) and infer empirical finite frequency kernels for surface waves (Lin and Ritzwoller, 2010).

The pace of these developments has been accelerated by the fact that once a surface wave EGF has been estimated by cross-correlating long time series of ambient noise recorded at a pair of stations, traditional methods of surface wave measurement, tomography, and inversion designed for application to earthquake records can be brought to bear on the result. These methods, however, largely have been developed to apply to observations obtained at single seismological stations. In this paper, we discuss a new method to utilize ambient noise within the context of a large-scale array such as the EarthScope USArray Transportable Array (Fig. 1), temporary deployments of large numbers of seismometers such as PASSCAL and USArray Flexible Array experiments, and international analogs of the US efforts (e.g., the Virtual European Broadband Seismograph Network, the rapidly growing seismic infrastructure in China sometimes referred to as ChinArray, and so on). Such extensive seismic arrays increasingly are becoming the preferred means to image high-resolution earth structures, and new methods are needed to exploit their capabilities.

The ambient noise array methods that are discussed here still are based on the computation of EGFs between every pair of stations in the array and the measurement of inter-station phase travel times as a function of period (Bensen et al., 2007). Time domain (Bensen et al., 2007) and spatial autocorrelation (Ekström et al., 2009) methods yield similar travel time estimates (Tsai and Moschetti, 2010). However, for each target station, the set of EGFs to all other stations is used to compute the travel time field of the surface wavefield across a map encompassing the array. In this case, the eikonal equation (Shearer, 2009) can be used to estimate the wave slowness and apparent direction for every location on the map. At each location and frequency, measurements from different target stations can be combined to estimate the azimuthal dependence of the wave speed, which allows an estimate of isotropic and azimuthally anisotropic velocities with rigorous uncertainties. We refer to this procedure as "eikonal tomography" (Lin et al., 2009) because of its basis in the eikonal equation. Eikonal tomography is described in section 2, as are results of its application to data from the EarthScope USarray across the western US. Examples of 3D Vs model results across the western US determined from ambient noise are contained in section 3.

There are several advantages of eikonal tomography compared with traditional tomographic methods (Barmin et al., 2001). Eikonal tomography accounts for ray bending but is not iterative, naturally generates uncertainties at each location in the tomographic maps, provides a direct (potentially visual) means to evaluate the azimuthal dependence of wave speeds, applies no ad hoc regularization because no inversion is performed, and is computationally very fast. There are approximations, however. The method is based on 2D wave propagation stemming from its background in the 2D wave equation, discards a term from the equation that accounts for finite frequency effects, and the method is essentially ray theoretic. We present evidence in section 4 that discarding the amplitude dependent term to derive the eikonal equation is justified at the periods where ambient noise tomography is typically performed (< 40 s). The theoretical background for many of the results presented here is described in greater detail by Lin et al. (2009, 2011a) and Lin and Ritzwoller (in press a,b).

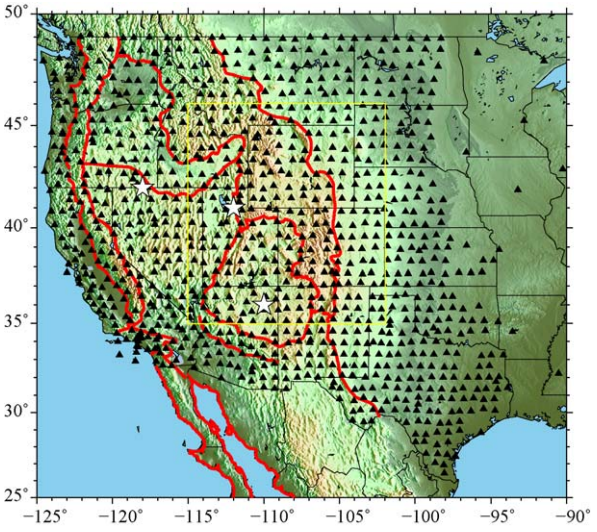

Fig. 1. There are 1021 EarthScope USArray Transportable Array and Permanent Array stations (black triangles) used in this study. Locations of geographical points for data results presented in the paper are shown with stars, red contours denote tectonic regions, and the yellow rectangle outlines the location of the results shown on Fig. 11.

Fig. 1. Il y a 1021 stations des *Earthscope USArray*, *Transportable Array* et *Permanent Array* (triangles noirs) utilisées dans cette étude. Les localisations des points géographiques dont les données sont présentées dans l'article sont représentées par des étoiles. Les contours rouges matérialisent les régions tectoniques, et le rectangle jaune, la zone d'où proviennent les résultats présentés sur la Fig. 11.

2. Eikonal tomography

Shearer (2009) shows that from the 2D scalar wave equation, the modulus of the gradient of the wave travel time $T\left(\vec{x}\right)$ is

$$|\nabla T|^2 = \frac{1}{c^2} + \frac{\nabla^2 A}{A\,\omega^2} \tag{1}$$

where $A\left(\vec{x}\right)$ is position dependent wave amplitude, ω is wave frequency, and c is wave phase speed. At high frequencies, thus in the ray theoretic limit, the second term on the right side of Eq. (1) can be ignored, the local direction of ray propagation can be identified with the direction of the gradient term, and the eikonal equation can be written in vector form as

$$\nabla T = \frac{\hat{k}}{c} \tag{2}$$

where $\hat{k}$ is the unit vector in the direction of ray propagation. Lin et al. (2009) and others (Langston and Liang, 2008) have shown how Eq. (2) can be used tomographically. Justification for and the consequences of dropping the second term on the right in Eq. (1) are discussed in section 4. The importance of retaining this term in earthquake tomography is discussed by Lin and Ritzwoller (in press a,b).

The eikonal tomography method is based on computing the gradient of the observed travel time surfaces, $T\left(\vec{x}\right)$, across a seismic array and is similar in many respects to other methods that track wavefronts (Langston and Liang, 2008; Pollitz, 2008; Pollitz and Snoke, 2010). In so doing, estimates of the local wave slowness ($1/c$) and the direction of ray propagation emerge immediately from Eq. (2). An example for the 24 s Rayleigh wave phase travel time surface across the western US centered on target station (USArray, Transportable Array) Q16A is shown in Fig. 2. The local apparent phase speed (or "dynamic phase speed" after Wielandt, 1993) and ray direction inferred from the gradient of this travel time map is presented in Fig. 3. Similar maps of phase speed and direction are derived from every other station in the array, which allows for the construction at each point across the map of estimates of wave speed versus azimuth of propagation. The mean and the standard deviation of the mean of all phase speed measurements are used to estimate local isotropic phase speed c_0 and its uncertainty.

To estimate azimuthal anisotropy for each location, all measurements from the nine nearby grid nodes with 0.6°C separation (3 × 3 grid with target point at the centre) are

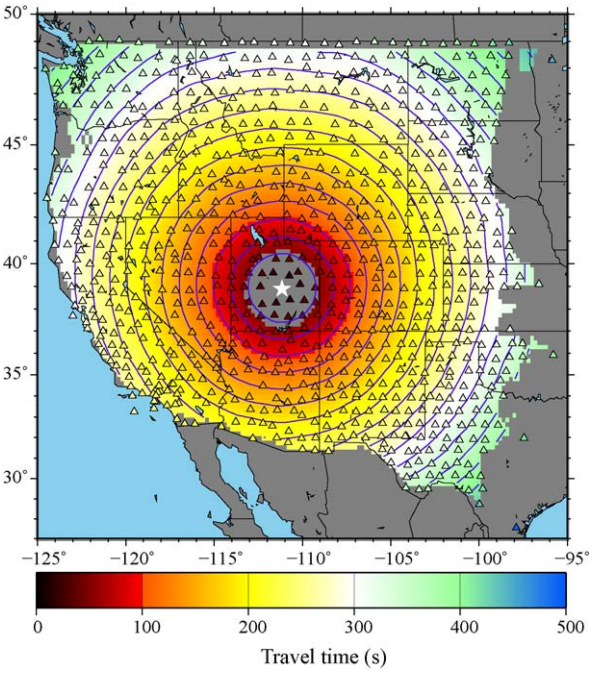

Fig. 2. The 24 s Rayleigh wave phase travel time surface computed from ambient noise empirical Green's functions across the western US based on central station (USArray, Transportable Array) Q16A in Utah. Travel time lines are presented in increments of wave period. The map is truncated within two wavelengths of the central station and where the travel times are not well determined. Station Q16A operated simultaneously with the 843 stations shown, but only for a short time near the western and eastern boundaries of the map.

Fig. 2. Surface d'isovaleur des temps de trajet de la phase d'onde de Rayleigh à 24 s, calculée d'après les fonctions de Green empiriques du bruit ambiant, à travers l'Ouest des État-Unis, et basée sur la station centrale Q16A dans l'Utah (*USArray*, *Transportable Array*). Les lignes de valeur du temps de trajet sont présentées par incrémentation d'une période de l'onde. La carte est tronquée dans deux longueurs d'onde autour de la station centrale et là où les trajets temporels ne sont pas bien déterminés. La station Q16A fonctionne simultanément avec les 843 présentées, mais seulement pour une période courte près des limites occidentale et orientale de la carte.

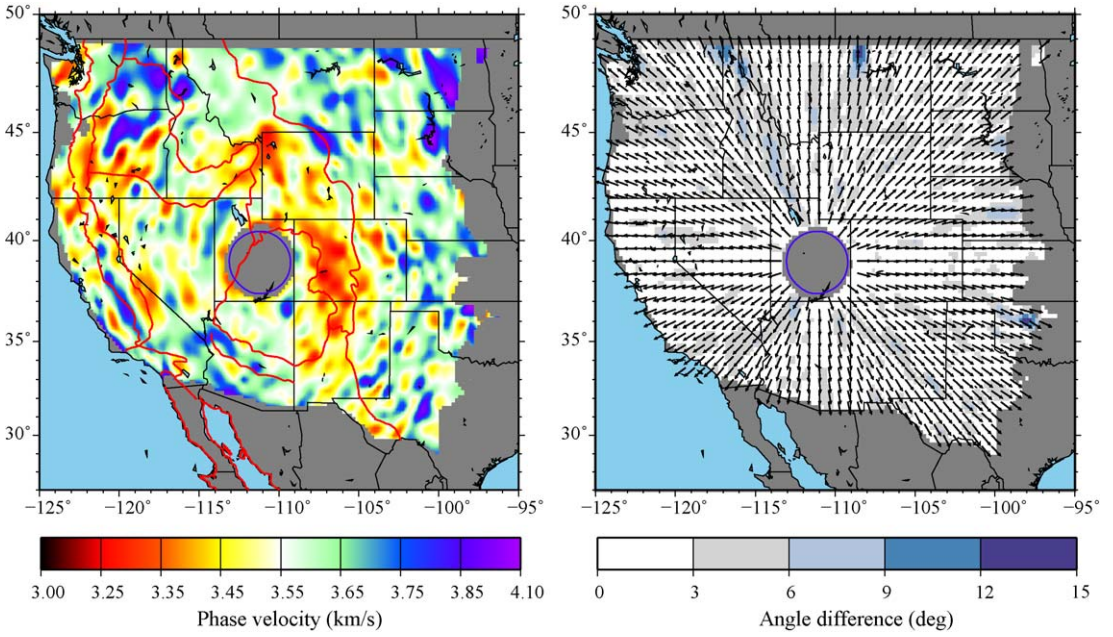

Fig. 3. The local (a) phase speed and (b) ray direction inferred from the gradient of the 24 s period Rayleigh wave travel time map shown on Fig. 2 for central TA station Q16A. In (b), the angular difference between the observed and radial directions is shown with the background colour.

Fig. 3. Vitesse locale de phase (a) et (b) direction du rayonnement déduite du gradient de la carte de trajet temporel de l'onde de Rayleigh à la période de 24 s, présentée sur la Fig. 2, pour la station centrale TA Q16A. En (b), la différence entre directions radiales et observées est matérialisée par la couleur du fond de la figure.

combined to estimate the azimuthal variation of the phase speeds. This is shown for two locations in Fig. 4 in which measured speeds are averaged in each 20°C azimuthal bin and plotted as 1σ (standard deviation) error bars. These error bars derive from the scatter in the measurements across nine adjacent grid nodes and provide a rigorous estimate of the random component of uncertainty in the phase speed as a function of azimuthal angle ψ. Based on theoretical expectations for a weakly anisotropic medium (Smith and Dahlen, 1973) and the observation of 180° periodicity in the azimuthally dependent phase speed measurements (e.g., Fig. 4), we fit, as a function of position and frequency, the following functional form to the observed variation of wave speed with azimuth

$$c(\psi) = c_0' + A\cos[2(\psi - \varphi)] \quad (3)$$

where c_0' is the isotropic wave speed, A and φ are the amplitude and fast direction of the 2ψ anisotropy, and where the angle ψ is measured positive clockwise from north. Thus, at each point on the map (at each

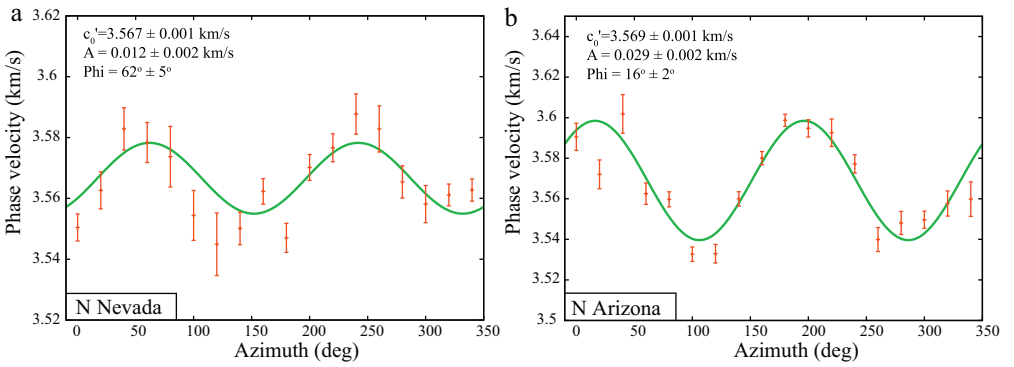

Fig. 4. Phase speeds as a function of azimuthal angle and averaged in each 20° bin for the 24 s Rayleigh wave are plotted as 1σ (standard deviation) error bars for example points in (a) Nevada (242°E, 42°N) and (b) Arizona (250°E, 36°N), identified with stars on Fig. 1. The best-fitting 2ψ curve (Eq. (3)) is presented as the green line in each panel. Estimated values with 1 standard deviation errors for c_0', A and φ are listed at upper left in each panel. The 2ψ component of anisotropy is clear in both panels.

Fig. 4. Les vitesses de phase en tant que fonction de l'azimut, et moyennées tous les 20° pour l'onde de Rayleigh à 24 s sont représentées avec des barres d'erreurs d'1σ (écart type) pour des points choisis au Nevada (242°E, 42°N) et en Arizona (250°E, 36°N) et matérialisés par des étoiles sur la Fig. 1. La courbe 2ψ de meilleur ajustement (Eq. (3)) est représentée, dans chaque panneau, par la ligne verte. Les valeurs estimées, avec des erreurs d'un écart type, pour c_0', A et φ sont listées à la partie supérieure gauche de chaque panneau. La composante 2ψ d'anisotropie est nette dans les deux panneaux.

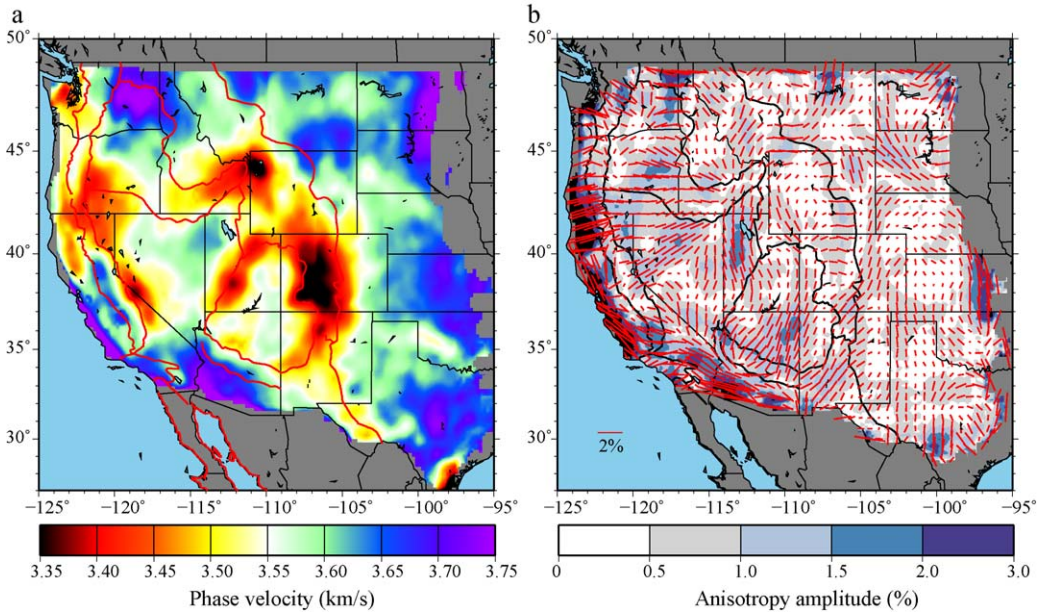

Fig. 5. (a): the 24 s Rayleigh wave isotropic phase speed map taken from ambient noise by averaging all local phase speed measurements at each point on the map; (b): the amplitudes and fast directions of the 2ψ component of the 24 s Rayleigh wave phase velocities. The amplitude of anisotropy is identified with the length of the bars, which point in the fast-axis direction, and is colour-coded in the background. At 24 s period, Rayleigh wave anisotropy reflects conditions in a mixture of the crust and uppermost mantle.

Fig. 5. (a) : carte de vitesse de phase isotrope de l'onde de Rayleigh à 24 s, obtenue à partir du bruit ambiant, en moyennant toutes les mesures locales de vitesse de phase à chaque point de la carte ; (b) : amplitudes et directions rapides de la composante 2ψ des vitesses de l'onde de Rayleigh à 24 s. L'amplitude de l'anisotropie est déterminée par la longueur des barres qui pointent dans la direction d'axe rapide, et est indiquée en couleur dans le fond de la figure : à la période de 24 s, l'anisotropie de l'onde de Rayleigh reflète des conditions de mélange de la croûte et de la partie la plus externe du manteau.

frequency) the quantities c_0', A, and φ are estimated together with their uncertainties. Note that c_0' and c_0 may differ slightly due to the nine point spatial averaging where c_0' provides a lower uncertainty but also lower resolution estimate.

When measurements of phase slowness and propagation direction are taken simultaneously from all of the stations across USArray, much more stable results emerge than those that appear in Fig. 3a. For example, the 24 s Rayleigh wave isotropic phase speed map (c_0) is shown in

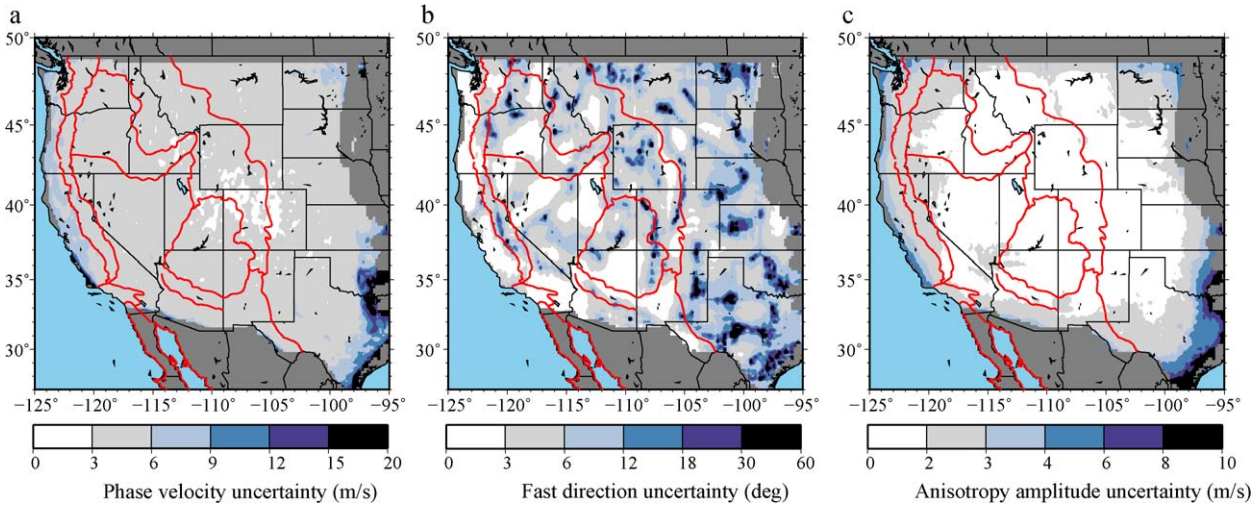

Fig. 6. Uncertainties in (a) the isotropic Rayleigh wave phase speed in metre per second, (b) the 2ψ fast-axis direction in degrees, and (c) the amplitude of the 2ψ component of anisotropy (in m/s) for the 24 s Rayleigh wave. Uncertainties are estimated at each point based on the scatter of measurements over azimuth and by fitting Eq. (3) to results such as those shown on Fig. 4.

Fig. 6. Incertitudes de la vitesse de phase isotrope de l'onde de Rayleigh en mètre par seconde (a), la direction d'axe rapide 2ψ en degrés (b) et l'amplitude de la composante 2ψ d'anisotropie en mètre par seconde (c), pour l'onde de Rayleigh à 24 s. Les incertitudes sont estimées à chaque point, en se basant sur la dispersion des mesures sur l'azimuth et par l'ajustement de l'Eq. (3) aux résultats tels que ceux présentés sur la Fig. 4.

Fig. 5a and the amplitudes (A) and fast directions (φ) of the 2ψ component of anisotropy are shown in Fig. 5b. Figs. 3a and 5a should be contrasted. No explicit smoothing or damping has been applied in constructing Fig. 5a. The greater smoothness of Fig. 5a compared with Fig. 3a results from averaging all the measurements at each point (from different central stations) over azimuth. Spatial variations of the azimuthal anisotropy are also smooth and amplitudes typically rise only to several percent. Examples of uncertainties in the variables (c_0, A, and φ) are shown in map form for the 24 s Rayleigh wave in Fig. 6. These matters are described in greater detail by Lin et al. (2009).

3. Inversion for isotropic and azimuthally anisotropic 3D Vs models

Isotropic and azimuthally anisotropic dispersion maps and uncertainties, such as those shown in Figs. 5 and 6, provide data to infer a 3D model of shear wave speeds within the earth. The vertical resolution and depth extent of the model will depend on the frequency band of the measurements. Ambient noise tomography typically produces maps to periods as short as 6 to 8 s, although shorter period maps have been constructed in some studies (Yang et al., 2011). This means that structures in

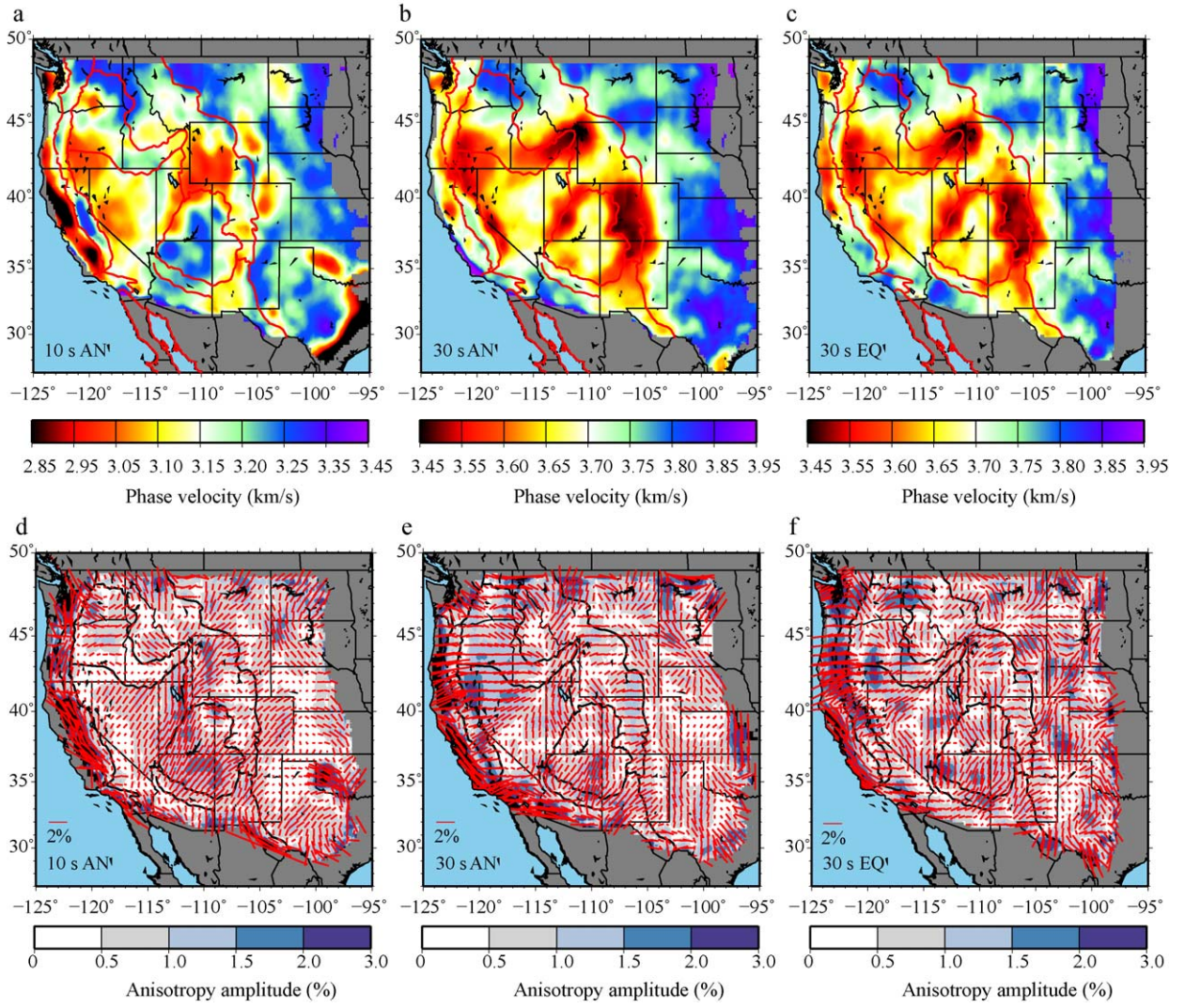

Fig. 7. (a) and (b): isotropic maps for the 10 s and 30 s period Rayleigh wave phase speed observed via eikonal tomography applied to ambient noise by averaging all measurements at each location, similar to Fig. 5a; (d) and (e): azimuthal anisotropy from ambient noise also at 10 s and 30 s period, similar to Fig. 5b; (c) and (f): maps of the isotropic Rayleigh wave speed and azimuthal anisotropy at 30 s period observed from teleseismic earthquakes via eikonal tomography (Lin and Ritzwoller, in press a), presented for comparison with (b) and (e).

Fig. 7. Cartes isotropes (a) et (b) de la vitesse de phase de l'onde de Rayleigh à 10 s et 30 s, observée par tomographie de l'eikonal, appliquée au bruit ambiant, en moyennant toutes les mesures à chaque localisation, comme en Fig. 5a ; (d) et (e) : anisotropie azimuthale à partir du bruit ambiant pour les périodes 10 s et 30 s, comme sur la Fig. 5b ; (c) et (f) : cartes de vitesse de l'onde isotrope de Rayleigh et d'anisotropie azimuthale à la période de 30 s, observées à partir de tremblements de terre télésismiques par tomographie de l'eikonal (Lin et Ritzwoller, sous presse a), présentées pour comparaison avec (b) et (e).

the shallow crust (top 5–10 km) can be resolved. Ambient noise tomography, however, rarely extends to periods above 30 to 40 s at regional scales, although long baseline measurements do extend to much longer periods (Bensen et al., 2008, 2009). The variation of the azimuthally dependent phase speed measurements increases dramatically at the longer periods. Thus, ambient noise alone typically constrains structures only to depths of 50 to 80 km. Deeper structures must be constrained with dispersion information from earthquakes as shown, for example, by Lin and Ritzwoller (in press b), Lin et al. (2011a), Moschetti et al. (2010a, 2010b) and Yang et al. (2008b).

Examples of Rayleigh wave phase speed maps from ambient noise at periods of 10 s and 30 s are shown in Fig. 7. Some of the features revealed by these maps have been observed before and were discussed previously by Lin et al. (2008), Moschetti et al. (2010a, 2010b), and Lin et al. (2011a). But the maps in Fig. 7 extend east of the Rocky Mountains, which now reveals new information about the transition from the tectonically deformed western US to the stable mid-continent region. Comparison with similar maps constructed using teleseismic earthquakes, such as those shown in Fig. 7c,f, plays an important role in establishing the reliability of the maps derived from ambient noise, both for isotropic (Yang and Ritzwoller, 2008) and azimuthally anisotropic variables. The 30 s period isotropic Rayleigh wave speeds in Fig. 7b (ambient noise) and Fig. 7c (earthquakes) differ on average by less than 0.1%, where the earthquake derived map is slightly faster, but the difference diminishes systematically as the number of earthquakes increases. The rms difference between these two isotropic maps is about 1%. The rms difference between the fast directions of azimuthal anisotropy determined from ambient noise and earthquakes for the 30 s map is about 25° and the standard deviation of differences in the amplitude of anisotropy is about 0.6%.

At 10 s period, several sedimentary basins clearly appear east of the Rocky Mountains: the Permian Basin in west Texas, the Anadarko Basin east of the Texas Panhandle, the Denver Basin in eastern Colorado, the Powder River Basin in eastern Wyoming, and the Williston Basin in western North Dakota. Although this region is on average faster than the western US, the maps display significant variability in the Great Plains even at 30 s period. Most of this variability at 30 s period is due to variations in crustal structure and thickness, which heretofore has been poorly understood. Love wave maps also have been constructed (Lin et al., 2008; Moschetti et al., 2010a), but are not shown here.

Both linearized (Yang et al., 2008a, 2008b) and Monte-Carlo (Lin et al., 2011a; Moschetti et al., 2010a, 2010b; Shapiro and Ritzwoller, 2002) methods to invert local Rayleigh and Love wave dispersion curves for a 3D Vs model are now well established. Example local dispersion curves for a point in northern Nevada are presented in Fig. 8. These include the anisotropic dispersion curves (Fig. 8b,c) discussed by Lin et al. (2011a). In these curves, below 25 s period ambient noise measurements are used alone, between 25 s and 45 s period, ambient noise and earthquake measurements are averaged, and above 45 s period earthquake measurements are used alone. At this location and many others across the western US, measurements of Rayleigh wave anisotropic amplitude and fast direction differ between short and long periods. This indicates that anisotropy differs between the crust and uppermost mantle, but these curves can be fit by a model in which crustal and uppermost mantle anisotropy are simple but distinct. Examples of crustal and uppermost mantle isotropic Vs wave speeds and azimuthal anisotropy are shown in Fig. 9, which is discussed in detail by Lin et al.

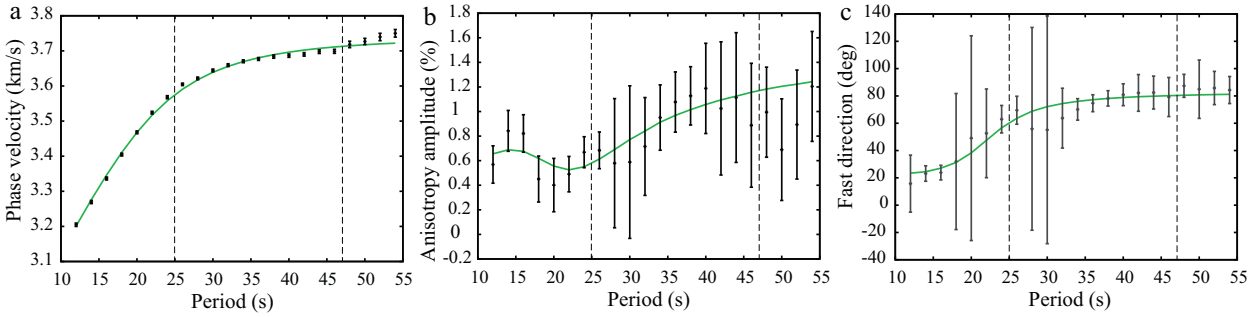

Fig. 8. Isotropic and azimuthally anisotropic dispersion curves in northern Nevada for the location shown with a star in Fig. 1. Only ambient noise measurements are used at periods below 25 s, ambient noise and earthquake measurements are averaged between 25 s and 45 s period, and only earthquake measurements are used above 45 s period. Phase velocity is presented in km/s, anisotropy amplitude in percent, and the fast direction of anisotropy in degrees east of north. Measurement uncertainties are presented with one standard deviation error bars. Additional scaling as described in Lin et al. (in press) is applied to the uncertainties of anisotropy measurements based on the misfit to the data by Eq. (3). The best-fitting curves based on the isotropic and anisotropic inversions are presented as the continuous line in each panel.

Fig. 8. Courbes de dispersion isotrope et azimuthalement anisotrope dans le Nord du Nevada, repéré par une étoile sur la Fig. 1. Seules les mesures de bruit ambiant sont utilisées aux périodes de moins de 25 s, les mesures de bruit ambiant et de tremblements de terre sont moyennées pour les périodes entre 25 et 45 s, et seules les mesures de tremblements de terre sont utilisées pour les périodes de plus de 45 s. La vitesse de phase est donnée en km/s, l'amplitude de l'anisotropie en pourcent, et la direction rapide d'anisotropie en degrés vers l'est depuis le nord. Les incertitudes dans les mesures sont présentées par des barres d'erreur d'un écart type. Une normalisation additionnelle, comme celle décrite par Lin et al. (in press) est appliquée aux incertitudes des mesures d'anisotropie, basées sur leur inadaptation aux données par rapport à l'Eq. (3). Les courbes de meilleur ajustement, basées sur les inversions isotropes et anisotropes sont représentées par une ligne dans chaque panneau.

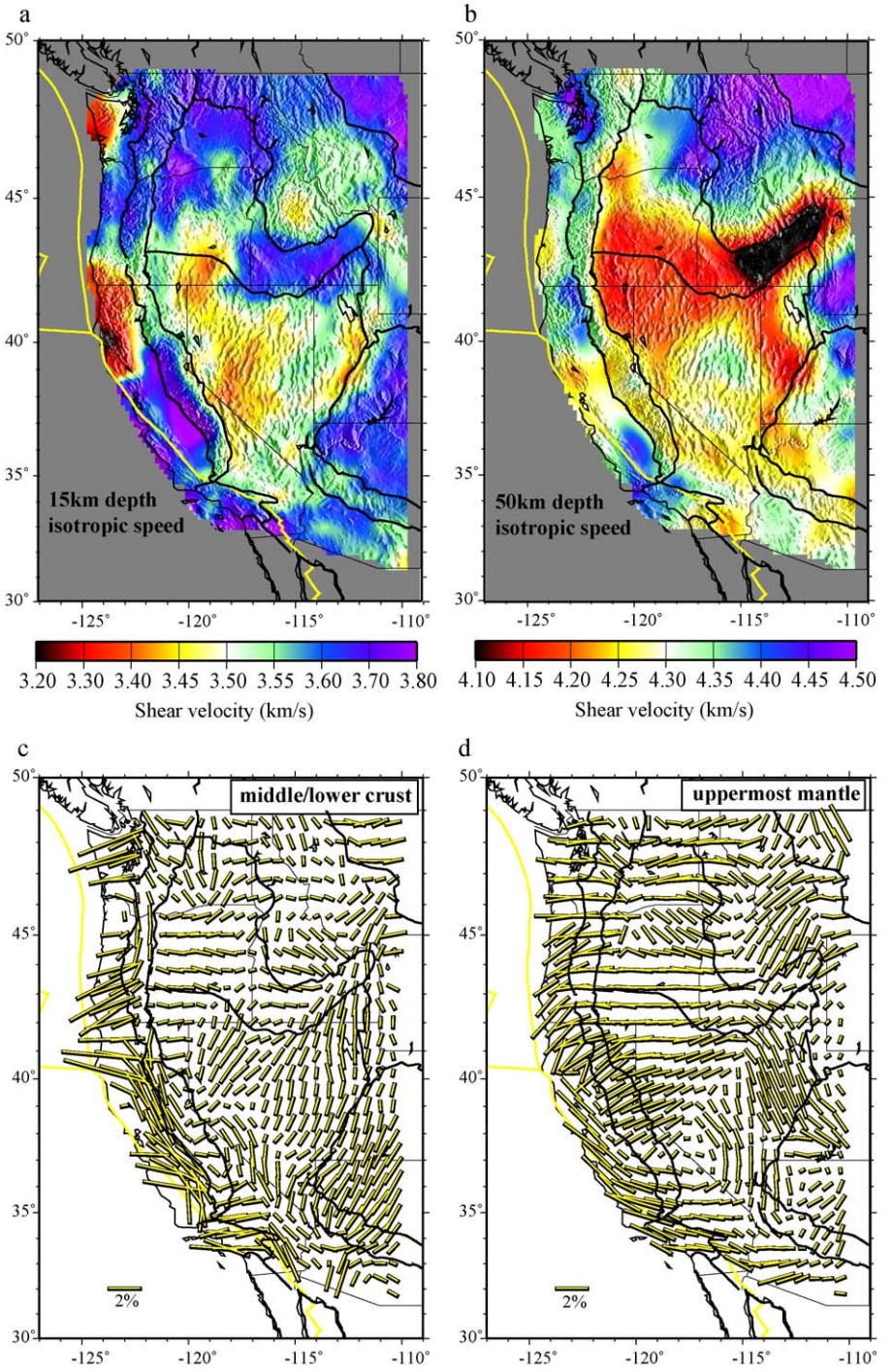

Fig. 9. 3D model results: (a): isotropic Vs velocity in the crust; (b): isotropic Vs velocity in the uppermost mantle; (c): azimuthal anisotropy in the middle to lower crust; and (d): anisotropy in the uppermost mantle. Results are taken from the model of Lin et al. (2011a).

Fig. 9. Résultats du modèle 3D : (a) : vitesse isotrope Vs dans la croûte ; (b) : vitesse isotrope Vs dans le manteau supérieur ; (c) : anisotropie azimuthale dans la partie moyenne et inférieure de la croûte ; (d) : anisotropie dans le manteau supérieur. Les résultats sont extraits du modèle de Lin et al. (2011a).

(2011a). Uncertainty estimates for these model parameters derive from the Monte-Carlo inversion.

4. The effect of approximations

The derivation of the eikonal equation, Eq. (2), involves discarding the Laplacian term $\nabla^2 A \,/\, A\omega^2$. This may be justified by considering it to be a ray theoretic (high frequency) approximation, but may also be valid if the amplitude field were sufficiently smooth; for example, if the length scale of the tomography is sufficiently large or isotropic structures are sufficiently smooth in the region. Thus, for global scale applications, rejection of this term may be justified. But, in ambient noise tomography, spatial length-scales are typically regional or local, not global (This is also increasingly true in earthquake studies; Lin and Ritzwoller, in press a,b; Pollitz, 2008; Pollitz and Snoke, 2010; Yang and Forsyth, 2006; Yang et al., 2008b). For this reason, in ambient noise tomography, the validity of the rejection of the Laplacian term will depend on the local smoothness of the medium and also will be frequency dependent.

To determine the relative size of the Laplacian term compared with the first (gradient) term on the right of Eq. (1), it would be best to compute it from amplitude observations just as the gradient term is computed from travel time observations. This is not so simple, however. In processing ambient noise (Bensen et al., 2007), amplitudes are typically normalized in the time domain by a running mean or one-bit normalization and spectra are commonly whitened. In addition, the amplitude of the ambient noise wavefield is neither isotropic nor stationary, but depends on excitation that varies with azimuth and season. Although, in principle, processing artifacts can be overcome or circumvented (Lin et al., in press; Prieto et al., 2009), doing so is beyond the scope of this paper.

The rejection of the Laplacian term, however, has an effect on apparent phase (or travel time) information that can be discerned in the observed azimuthal distribution of apparent phase speeds. Lin and Ritzwoller (in press a) discuss this in detail for earthquake data and show that discarding this term introduces an apparent 1ψ bias in the azimuthal distribution of phase speeds in regions with strong lateral structural gradients. Although their discussion is for earthquake waves, the physical significance of the Laplacian term is the same for ambient noise wavefields. Thus, observation of a 1ψ term in the azimuthal distribution of phase speeds is evidence that the Laplacian term may be important for the fidelity of both the isotropic and anisotropic components of local phase velocity. Conversely, lack of observation of a 1ψ component is evidence that the Laplacian term and, thus, isotropic bias of inferred anisotropy is small and the use of the eikonal equation is justified.

Lin and Ritzwoller (in press a) discuss how backscattering near strong structural contrasts causes the 1ψ term. The details of the effect will depend on the shape of the anomaly, so smaller bias terms may also exist for the 0ψ, 2ψ, 3ψ, etc. components of local phase speed as Bodin and Maupin (2008) discuss. To diagnose the presence of a 1ψ term, we modify Eq. (3) to include the term $A_{1\psi}\cos[\psi - \alpha]$, where α is the fast direction and $A_{1\psi}$ is the amplitude of the 1ψ component.

Fig. 10 presents examples of the apparent distribution of phase speed as a function of azimuth for periods of 10 s, 30 s, and 60 s for a point in northern Utah based on eikonal tomography with ambient noise measurements. At 10 s and 30 s periods, only the 2ψ component is strong. However, at 60 s period, in addition to larger error bars due to the stronger scatter caused by lower signal-to-noise ratio at longer periods for ambient noise, the 1ψ component is dominant and is much stronger than the 2ψ component at any period. While lower signal-to-noise ratios at longer periods can prevent the extraction of meaningful 2ψ azimuthal anisotropy information, the existence of strong 1ψ signal is evidence of systematic bias in estimates of both isotropic and anisotropic variables. The size of the observed 1ψ component across the centre of

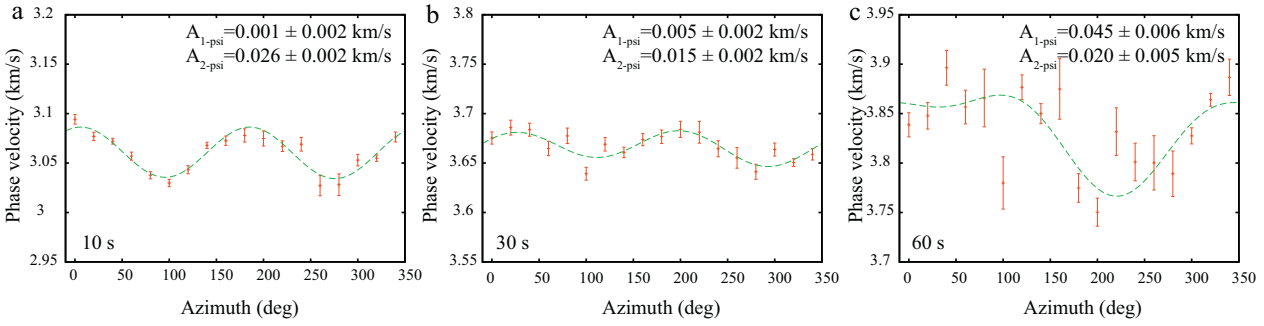

Fig. 10. Rayleigh wave phase speeds determined from ambient noise as a function of azimuthal angle and averaged in each 20° azimuthal bin are plotted as 1σ (standard deviation) error bars at periods of 10 s, 30 s, and 60 s for the point in northern Utah shown with a star on Fig. 1. The green dashed line is the best fitting 1ψ and 2ψ curve. The 1ψ component is small at periods below ~40 s, but dominates the azimuthal dependence of phase velocities at 60 s period. The 1ψ component is spurious, resulting from the apparent phase velocity increase or decrease caused by backscattering near the station.

Fig. 10. Les vitesses de phase de l'onde de Rayleigh, déterminées à partir du bruit ambiant comme une fonction de l'angle azimuthal et moyennées tous les 20° sur l'azimuth, sont représentées avec des barres d'erreur d'1σ (déviation standard) pour les périodes 10, 30 et 60 s sur l'exemple du Nord de l'Utah matérialisé par une étoile sur la Fig. 1. La ligne verte en tiretés représente le meilleur ajustement des courbes 1ψ et 2ψ (Eq. (3)). La composante 1ψ est faible pour les périodes au-dessous de 40 s, mais domine la dépendance azimuthale de vitesses de phase pour la période de 60 s. La composante 1ψ est parasite, résultant de la croissance ou de la décroissance apparente de la vitesse de phase causée par la rétrodiffusion près de la station.

our study region, where we have measurements from all azimuths and isotropic structures are particularly complex, is shown on Fig. 11 at several periods. The amplitude of this component is small at 10 s and 30 s period even though isotropic anomalies are strong. At 60 s period, however, the 1ψ component has a large amplitude surrounding many of the prominent isotropic velocity anomalies (Fig. 11c,f). Around low velocity anomalies, such as the Snake River Plain anomaly seen in the 60 s map in Fig. 11c, the fast directions of the 1ψ component point radially outward from the isotropic anomaly. Around high velocity anomalies, such as that in Wyoming (Fig. 11c), the fast directions of the 1ψ component point radially inward toward the isotropic anomaly. This provides the diagnosis that the 1ψ signal arises from backscattering in the neighbourhood of a velocity contrast.

The observation of a gradual increase of the 1ψ component of Rayleigh wave phase velocities at periods above about 40 s is evidence for systematic bias in estimates of isotropic and anisotropic structures. Thus, above 50 s period, ignoring the Laplacian term in eikonal tomography is invalid in regions with strong lateral

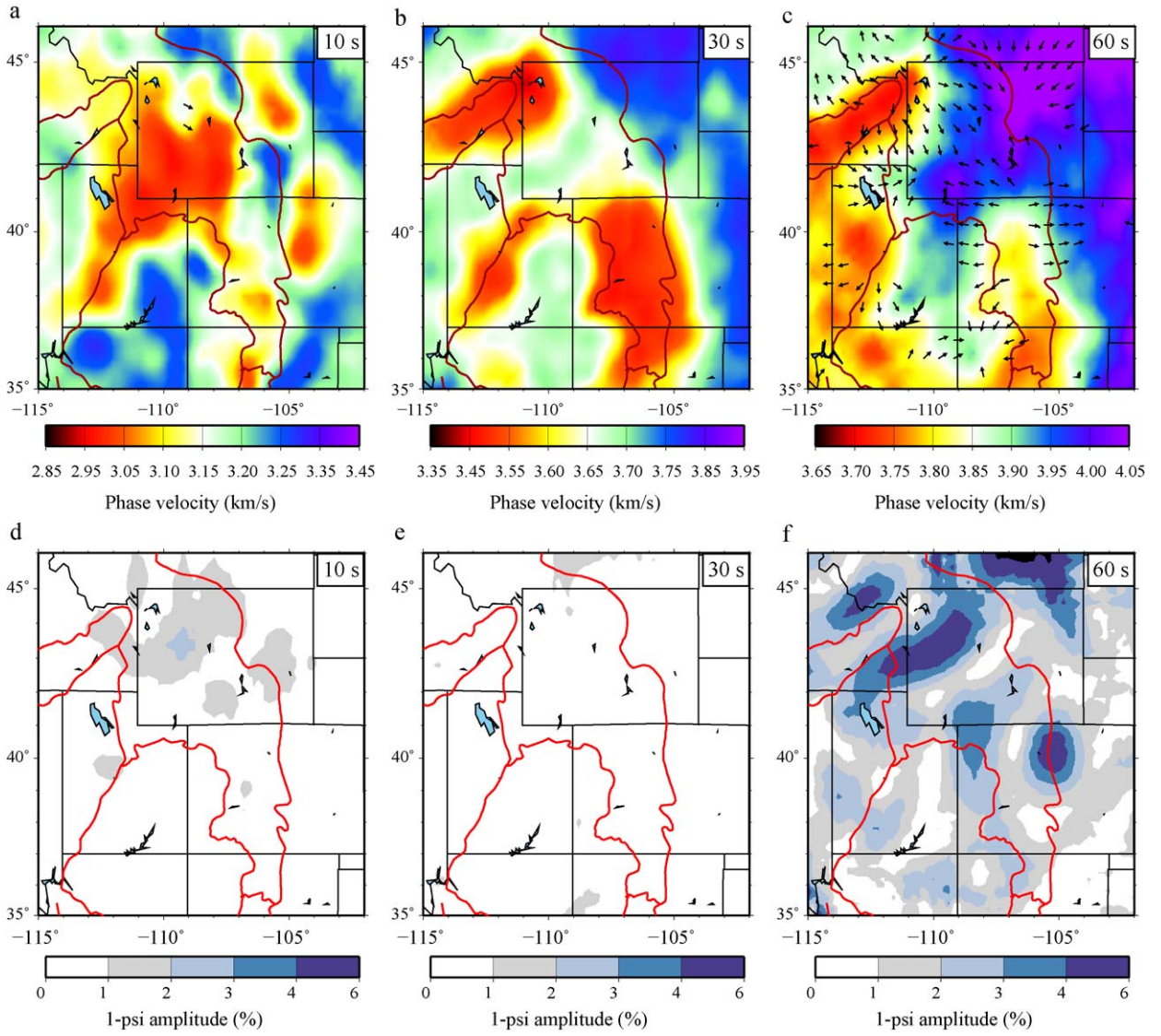

Fig. 11. (a)–(c): maps of isotropic Rayleigh wave speeds at 10 s, 30 s, and 60 s period (presented in km/s) determined from ambient noise where the orientation of the 1ψ component of Rayleigh phase speed is over-plotted with an arrow pointing in the fast-direction. Arrows are plotted only if the peak-to-peak amplitude of the 1ψ component is at least 2%. At 60 s, arrows point away from slow isotropic anomalies and toward fast anomalies. (d)–(f) Amplitude of the 1ψ component of phase speed, presented in percent. Strong amplitudes surround the principal isotropic anomalies at 60 s period.

Fig. 11. (a)–(c) : cartes de vitesses isotropes de l'onde de Rayleigh aux périodes de 10, 30 et 60 s (présentées en km/s), déterminées à partir du bruit ambiant. L'orientation de la composante 1ψ de la vitesse de phase de Rayleigh est sur-ajoutée, avec une flèche pointant dans la direction rapide. Les flèches sont représentées seulement si l'amplitude pic-à-pic de la composante 1ψ est au moins de 2 %. À 60 s, les flèches s'écartent des anomalies isotropes lentes et pointent vers les anomalies rapides. (d)–(f) : amplitude de la composante 1ψ de la vitesse de phase, donnée en pourcent. Les fortes amplitudes entourent les anomalies isotropes principales pour la période 60 s.

gradients in the isotropic wave speeds. Below 40 s period, which is the focus of most ambient noise studies, the 1ψ term is largely negligible, even where structural gradients are exceptionally strong. The introduction of measurements obtained from earthquakes (Lin et al., 2011a) helps to reduce uncertainties in the directionally dependent phase speed measurements and improves the azimuthal coverage particularly near the periphery of the map. It does not mitigate the near-station backscattering effect at periods above 50 s, however (Lin and Ritzwoller, in press a). It is possible and considerably easier to retain the Laplacian term in Eq. (1) for earthquake measurements, because of the loss of amplitude information in obtaining ambient noise measurements. Thus, in the context of regional scale structures such as those resolved in the western US, above 50 s period the Laplacian term in Eq. (1) should be retained to ensure the accuracy of the amplitude of isotropic structures and to minimize bias in the 2ψ component of azimuthal anisotropy. This is done for earthquakes waves by Lin and Ritzwoller (in press b).

5. Conclusions

The development and growth of dense, large-scale seismic continental arrays, such as deployments that are now in place in China, Europe, and the US (e.g., EarthScope USarray), present the unprecedented opportunity to map the substructure of continents at a resolution that appeared to be impossible before their deployment. To capitalize on the investments that these and similar arrays represent, new methods of seismic tomography need to be developed to wring from the arrays more information, better information, and qualitative and quantitative assessments of the accuracy of the information. We present here a discussion of one such method, called eikonal tomography, which is designed to exploit information contained in surface waves that compose ambient noise. We argue that the eikonal tomography method extracts information from ambient noise at high resolution about isotropic wave speeds as well as azimuthal anisotropy at periods from less than 10 s to about 40 s. The information at the short period end of this band often provides unique constraints on crustal structure as surface waves below 20 s period are difficult to observe in many locations with earthquake sources and teleseismic body wave do not determine crustal structures well. In addition, eikonal tomography provides meaningful uncertainty estimates about all measured quantities.

Perhaps the greatest challenge to face new methods designed to exploit the emerging continental arrays will be to mitigate the effects of complexities in the seismic wavefield on the inferred quantities. This is particularly true if relatively subtle influences on the wavefield, such as azimuthal anisotropy, are the intended inferred observable. In particular, wavepath bending or refraction, scattering and multipathing on the way to the array (for teleseismic earthquakes) which are often called non-planar wave effects, wavefield effects within the array (such as wavefront healing and backscattering near an observing station), and azimuthal variations in excitation of the wavefield all can affect the observed phase speed of the wavefield and introduce spurious or apparent effects unless they are accounted for explicitly in the data processing and inversion procedures.

Eikonal tomography explicitly tracks wavefields and, therefore, accounts for wavepath bending that is particularly important near sharp structural contrasts and at short periods. But, it is a ray theoretic method and, therefore, does not model structural or wavefield effects away from the ray. However, by its very nature, the inter-station ambient noise wavefield, in contrast with earthquakes, is free from effects external to the array. Wavefield complexities such as wavefront healing and near-station backscattering potentially are important for ambient noise, however, and eikonal tomography, defined by Eq. (2) here, does not explicitly account for it. We present evidence that below 40 s period imaging methods based on ambient noise can ignore wavefield complexities, such as wavefront healing and near-station back scattering. Above $\sim$50 s period, however, they become increasingly important both for ambient noise and earthquake wavefields. In this case, eikonal tomography will need to be modified to include the second term in Eq. (1), which is based on the amplitude of the observed wavefield. This Laplacian term is deceptively simple, but it accounts for a wide array of wavefield effects, including wavefield complexities arising within the array (or outside the array for earthquake observations) as well as azimuthal variations in excitation. Its application, however, requires that amplitudes be well defined so that instruments must be well calibrated and processing procedures cannot result in the degradation or loss of information about amplitudes.

The retention of the Laplacian term in Eq. (1) with earthquake data is relatively straightforward and is discussed by Lin and Ritzwoller (in press b). Standard ambient noise data processing, however, typically loses amplitude information. Therefore, to apply eikonal tomography above $\sim$50 s period and retain the Laplacian term in Eq. (1) will require that these procedures be modified so that, at the very least, the effects of data selection and of various normalizations in the time and frequency domain are understood and can be effectively undone. This is an area of active research and is discussed further by Lin et al. (in press). Another approach to model non-ray theoretic effects would be to employ empirical finite frequency sensitivity kernels. Lin and Ritzwoller (2010) describe such an approach in detail.

Acknowledgments

The authors thank two anonymous reviewers for constructive comments. Instruments [data] used in this study were made available through EarthScope (www.earthscope.org; EAR-0323309), supported by the National Science Foundation. The facilities of the IRIS Data Management System, and specifically the IRIS Data Management Centre, were used for access to waveform and metadata required in this study. The IRIS DMS is funded through the US National Science Foundation (NSF) and specifically the GEO Directorate through the Instrumentation and Facilities Program of the National Science

Foundation under Cooperative Agreement EAR-0552316. This work has been supported by NSF grants EAR-0711526 and EAR-0844097.

References

Arroucau, P., Rawlinson, N., Sambridge, M., 2010. New insight into Cainozoic sedimentary basins and Palaeozoic suture zones in southeast Australia from ambient noise surface wave tomography. Geophys. Res. Lett. 37, L07303.

Barmin, M.P., Ritzwoller, M.H., Levshin, A.L., 2001. A fast and reliable method for surface wave tomography. Pure Appl. Geophys. 158 (8), 1351–1375.

Barmin, M.P., Levshin, A.L., Yang, Y.M.H., 2011. Ritzwoller, Epicentral location based on Rayleigh wave empirical Green's functions from ambient seismic noise. Geophys. J. Int. 184 (2), 869–884.

Behr, Y., Townend, J., Bannister, S., Savage, M.K., 2010. Shear velocity structure of the Northland Peninsula, New Zealand, inferred from ambient noise correlations. J. Geophys. Res. Solid Earth 115, B05309.

Bensen, G.D., Ritzwoller, M.H., Barmin, M.P., Levshin, A.L., Lin, F., Moschetti, M.P., Shapiro, N.M., Yang, Y., 2007. Processing seismic ambient noise data to obtain reliable broad-band surface wave dispersion measurements. Geophys. J. Int. 169, 1239–1260.

Bensen, G.D., Ritzwoller, M.H., Shapiro, N.M., 2008. Broadband ambient noise surface wave tomography across the United States. J. Geophys. Res. 113 (B5), B05306 doi:10.1029/2007JB005248.

Bensen, G.D., Ritzwoller, M.H., Yang, Y., 2009. A 3D shear velocity model of the crust and uppermost mantle beneath the United States from ambient seismic noise. Geophys. J. Int. 177, 1177–1196.

Bodin, T., Maupin, V., 2008. Resolution potential of surface wave phase velocity measurements at small arrays. Geophys. J. Int. 172, 698–706.

Brenguier, F., Shapiro, N.M., Campillo, M., Nercessian, A., Ferrazzini, V., 2007. 3D surface wave tomography of the Piton de la Fournaise volcano using seismic noise correlations. Geophys. Res. Lett. 34 (2), L02305.

Cho, K.H., Herrmann, R.B., Ammon, C.J., Lee, K., 2007. Imaging the upper crust of the Korean Peninsula by surface-wave tomography. Bull. Seismol. Soc. Am. 97 (1), 198–207 Part B Sp. Iss. S.

Ekström, G., Abers, G.A., Webb, S.C., 2009. Determination of surface-wave phase velocities across USArray from noise and Aki's spectral formulation. Geophys. Res. Lett. 36, L18301.

Fang, L.H., Wu, J.P., Ding, Z.F., Panza, G.F., 2010. High resolution Rayleigh wave group velocity tomography in North China from ambient seismic noise. Geophys. J. Int. 181 (2), 1171–1182.

Gerstoft, P., Shearer, P.M., Harmon, N., Zhang, J., 2008. Global P, PP, and PKP wave microseisms observed from distant storms. Geophys. Res. Lett. 35 (23), L23306.

Gudmundsson, O., Khan, A., Voss, P., 2007. Rayleigh-wave group-velocity of the Icelandic crust from correlation of ambient seismic noise. Geophys. Res. Lett. 34 (14), L14314.

Guo, Z., Gao, X., Yao, H.J., Li, J., Wang, W.M., 2009. Midcrustal low-velocity layer beneath the central Himalaya and southern Tibet revealed by ambient noise array tomography. Geochem. Geophys. Geosys. 10, Q05007.

Harmon, N., Forsyth, D., Webb, S., 2007. Using ambient seismic noise to determine short-period phase velocities and shallow shear velocities in young oceanic lithosphere. Bull. Seismol. Soc. Am. 97 (6), 2009–2023.

Kang, T.S., Shin, J.S., 2006. Surface-wave tomography from ambient seismic noise of accelerograph networks in southern Korea. Geophys. Res. Lett. 33 (17), L17303.

Landes, M., Hubans, F., Shapiro, N.M., Paul, A., Campillo, M., 2010. Origin of deep ocean microseisms by using teleseismic body waves. J. Geophys. Res. Solid Earth 115, B05302.

Langston, C.A., Liang, C., 2008. Gradiometry for polarized seismic waves. J. Geophys. Res. 113, B08305 doi:10.1029/2007JB005486.

Li, H.Y., Su, W., Wang, C.Y., Huang, Z.X., 2009. Ambient noise Rayleigh wave tomography in western Sichuan and eastern Tibet. Earth Planet. Sci. Lett. 282 (1–4), 201–211.

Li, H.Y., Bernardi, F., Michelini, A., 2010. Surface wave dispersion measurements from ambient seismic noise analysis in Italy. Geophys. J. Int. 180 (3), 1242–1252.

Liang, C.T., Langston, C.A., 2008. Ambient seismic noise tomography and structure of eastern North America. J. Geophys. Res. Solid Earth 113 (B3), B03309.

Lin, F.C., Ritzwoller, M.H., 2010. Empirically determined finite frequency sensitivity kernels for surface waves. Geophys. J. Int. 182, 923–932 doi:10.1111/j.1365-246X.2010.0.4643.x.

Lin, F.C. and Ritzwoller, M.H., in press a. Apparent anisotropy in inhomogeneous isotropic media, Geophys. J. Int..

Lin, F.C. and Ritzwoller, M.H., in press b. Helmholtz surface wave tomography for isotropic and azimuthally anisotropy structure, Geophys. J. Int.

Lin, F.C., Ritzwoller, M.H., Townend, J., Bannister, S., Savage, M.K., 2007. Ambient noise Rayleigh wave tomography of new Zealand. Geophys. J. Int. 170, 649–666.

Lin, F.C., Moschetti, M.P., Ritzwoller, M.H., 2008. Surface wave tomography of the western United States from ambient seismic noise: Rayleigh and Love wave phase velocity maps. Geophys. J. Int. 173, 281–298.

Lin, F.C., Ritzwoller, M.H., Snieder, R., 2009. Eikonal tomography: surface wave tomography by phase front tracking across a regional broadband seismic array. Geophys. J. Int. 177, 1091–1110.

Lin, F.C., Ritzwoller, M.H., Yang, Y., Moschetti, M.P., Fouch, M.J., 2011a. Complex and variable crust and uppermost mantle seismic anisotropy in the western US. Nature Geosci. 4 (1), 55–61.

Lin, F.C., Ritzwoller, M.H. and Shen, W., in press. On the reliability of attenuation measurements from ambient noise cross correlations, Geophys. Res. Lett.

Moschetti, M.P., Ritzwoller, M.H., Shapiro, N.M., 2007. Surface wave tomography of the western United States from ambient seismic noise: Rayleigh wave group velocity maps. Geochem. Geophys. Geosys. 8, Q08010 doi:10.1029/2007GC001655.

Moschetti, M.P., Ritzwoller, M.H., Lin, F.C., 2010a. Seismic evidence for widespread crustal deformation caused by extension in the western USA. Nature 464 (N7290), 885–889.

Moschetti, M.P., Ritzwoller, M.H., Lin, F.C., Yang, Y., 2010b. Crustal shear velocity structure of the western US inferred from ambient noise and earthquake data. J. Geophys. Res. 115, B10306 doi:10.1029/2010JB007448.

Nishida, K., Kawakatsu, H., Obara, K., 2008. Three-dimensional crustal S wave velocity structure in Japan using microseismic data recorded by Hi-net tiltmeters. J. Geophys. Res. Solid Earth 113 (B10), B10302.

Nishida, K., Montagner, J.P., Kawakatsu, H., 2009. Global surface wave tomography using seismic hum. Science 326 (5949), 112–1112.

Pollitz, F.F., 2008. Observations and interpretation of fundamental mode Rayleigh wavefields recorded by the Transportable Array (USArray). Geophys. J. Int. 173, 189–204.

Pollitz, F.F., Snoke, J.A., 2010. Rayleigh-wave phase-velocity maps and three-dimensional shear velocity structure of the western US from local non-plane surface wave tomography. Geophys. J. Int. 180, 1153–1169.

Prieto, G.A., Lawrence, J.F., Beroza, G.C., 2009. Anelastic Earth structure from the coherency of the ambient seismic field. J. Geophys. Res. Solid Earth 114, B07303.

Roux, P., Sabra, K.G., Gerstoft, P., Kuperman, W.A., Fehler, M.C., 2005. P-waves from cross-correlation of seismic noise. Geophys. Res. Lett. 32 (19), L19303.

Sabra, K.G., Gerstoft, P., Roux, P., Kuperman, W.A., Fehler, M.C., 2005. Surface wave tomography from microseisms in southern California. Geophys. Res. Lett. 32, L14311.

Saygin, E., Kennett, B.L.N., 2010. Ambient seismic noise tomography of Australian continent. Tectonophysics 481, 116–125.

Shapiro, N.M., Campillo, M., 2004. Emergence of broadband Rayleigh waves from correlations of the ambient seismic noise. Geophys. Res. Lett. 31 (7), L07614.

Shapiro, N.M., Ritzwoller, M.H., 2002. Monte-Carlo inversion for a global shear velocity model of the crust and upper mantle. Geophys. J. Int. 151, 88–105.

Shapiro, N.M., Campillo, M., Stehly, L., Ritzwoller, M.H., 2005. High-resolution surface-wave tomography from ambient seismic noise. Science 307, 1615–1618.

Shearer, P., 2009. Introduction to Seismology. Cambridge University Press, Cambridge.

Smith, M.L., Dahlen, F.A., 1973. Azimuthal dependence of Love and Rayleigh-wave propagation in a slightly anisotropic medium. J. Geophys. Res. 78, 3321–3333.

Stachnik, J.C., Dueker, K., Schutt, D.L., Yuan, H., 2008. Imaging Yellowstone plume-lithosphere interactions from inversion of ballistic and diffusive Rayleigh wave dispersion and crustal thickness data. Geochem. Geophys. Geosys. 9, Q06004.

Stehly, L., Fry, B., Campillo, M., Shapiro, N.M., Guilbert, J., Boschi, L., Giardini, D., 2009. Tomography of the Alpine region from observations of seismic ambient noise. Geophys. J. Int. 178 (1), 338–350.

Sun, X., Song, X., Zheng, S., Yang, Y., Ritzwoller, M.H., 2010. Three-dimensional shear velocity structure of crust and upper mantle in China from ambient noise surface wave tomography. Earthquake Sci. 23, 449–463 doi:10.1007/s11589-010-0744-3.

Tsai, V.C., Moschetti, M.P., 2010. An explicit relationship between time-domain noise correlation and spatial autocorrelation (SPAC) results. Geophys. J. Int. 182, 454–460 doi:10.1111/j.1365-246X.2010.0,4633.x.

Villaseñor, A., Yang, Y., Ritzwoller, M.H., Gallart, J., 2007. Ambient noise surface wave tomography of the Iberian Peninsula: Implications for shallow seismic structure. Geophys. Res. Lett. 34, L11304 doi:10.1029/2007GL030164.

Wielandt, E., 1993. Propagation and structural interpretation of non-plane waves. Geophys. J. Int. 113, 45–53.

Yang, Y.J., Forsyth, D.W., 2006. Regional tomographic inversion of the amplitude and phase of Rayleigh waves with 2-D sensitivity kernels. Geophys. J. Int. 166, 1148–1160.

Yang, Y., Ritzwoller, M.H., 2008. Teleseismic surface wave tomography in the western US using the Transportable Array component of USArray. Geophys. Res. Lett. 5, L04308 doi:10.1029/2007GL032278.

Yang, Y.J., Ritzwoller, M.H., Levshin, A.L., Shapiro, N.M., 2007. Ambient noise Rayleigh wave tomography across Europe. Geophys. J. Int. 168 (1), 259–274.

Yang, Y.J., Li, A.B., Ritzwoller, M.H., 2008a. Crustal and uppermost mantle structure in southern Africa revealed from ambient noise and teleseismic tomography. Geophys. J. Int. 174, 235–248.

Yang, Y., Ritzwoller, M.H., Lin, F.-C., Moschetti, M.P., Shapiro, N.M., 2008b. Structure of the crust and uppermost mantle beneath the western United States revealed by ambient noise and earthquake tomography. J. Geophys. Res. Solid Earth 113, B12310.

Yang, Y., Zheng, Y., Chen, J., Zhou, S., Celyan, S., Sandvol, E., Tillmann, F., Priestley, K., Hearn, T.M., Ni, J.F., Brown, L.D., Ritzwoller, M.H., 2010. Rayleigh wave phase velocity maps of Tibet and the surrounding regions from ambient seismic noise tomography. Geochem. Geophys. Geosys. 11 (8), Q08010 doi:10.1029/2010GC003119.

Yang, Y., Ritzwoller, M.H., Jones, C.H., 2011. Crustal structure determined from ambient noise tomography near the magmatic centers of the Coso region, southeastern California. Geochem. Geophys. Geosyst. 12, Q02009 doi:10.1029/2010GC003362.

Yao, H.J., van der Hilst, R.D., de Hoop, M.V., 2006. Surface-wave array tomography in SE Tibet from ambient seismic noise and two-station analysis – I. Phase velocity maps. Geophys. J. Int. 166 (2), 732–744.

Yao, H.J., Beghein, C., van der Hilst, R.D., 2008. Surface wave array tomography in SE Tibet from ambient seismic noise and two-station analysis – II. Crustal and upper-mantle structure. Geophys. J. Int. 173 (1), 205–219.

Yao H., Campman, X., de Hoop, M.V., van der Hilst, R.D., 2009. Estimation of surface-wave Green's function from correlations of direct waves, coda waves, and ambient noise in SE Tibet, Phys. Earth Planet. Int. doi:10.1016/j.pepi.2009.07.002.

Yao, H., van der Hilst, R.D., Montagner, J.-P., 2010. Heterogeneity and anisotropy of the lithosphere of SE Tibet from surface wave array tomography. J. Geophys. Res. 115, B12307 doi:10.1029/2009JB007142.

Zhan, Z.W., Ni, S.D., Helmberger, D.V., Clayton, R.W., 2010. Retrieval of Moho-reflected shear wave arrivals from ambient seismic noise. Geophys. J. Int. 182 (1), 408–420.

Zheng, S.H., Sun, X.L., Song, X.D., Yang, Y.J., Ritzwoller, M.H., 2008. Surface wave tomography of China from ambient seismic noise correlation. Geochem. Geophys. Geosyst. 9, Q05020 doi:10.1029/2008GC001981.

Zheng, X.F., Jiao, W.J., Zhang, C.H., Wang, L.S., 2010a. Short-period Rayleigh-wave group velocity tomography through ambient noise cross-correlation in Xinjiang, Northwest China. Bull. Seismol. Soc. Am. 100 (3), 1350–1355.

Zheng, Y., Yang, Y., Ritzwoller, M.H., Zheng, X., Xiong, X., Li, Z., 2010b. Crustal structure of the northeastern Tibetan Plateau, the Ordos Block and the Sichuan Basin from ambient noise tomography. Earthquake Sci. 23, 465–476 doi:10.1007/s11589-010-0745-3.